Ru decorated TiO_x nanoparticles via laser bombardment for photothermal co-catalytic CO_2 hydrogenation to methane with high selectivity

Tianjiao Dong [a,d], Xiaoyu Liu [a,b], Zhenfei Tang [a], Haifeng Yuan [a], Di Jiang [a], Yijie Wang [a], Zhen Liu [a], Xiaoli Zhang [c], Shifeng Huang [d], Hong Liu [a,b], Lili Zhao [a,*], Weijia Zhou [a,*]

[a] Institute for Advanced Interdisciplinary Research (iAIR), School of Chemistry and Chemical Engineering, University of Jinan, Jinan 250022, PR China
[b] State Key Laboratory of Crystal Materials, Shandong University, Jinan 250100, PR China
[c] School of Materials Science and Engineering, Zhengzhou University, Zhengzhou 450001, PR China
[d] Shandong Provincial Key Laboratory of Preparation and Measurement of Building Materials, University of Jinan, Jinan 250022, PR China

ARTICLE INFO

ABSTRACT

The global warming makes us focus on the resource utilization of CO_2. Herein, defective TiO_x nanoparticles with rich oxygen vacancies are synthesized through laser bombardment, and uniform Ru nanoparticles are loaded on the TiO_x (Ru-TiO_x) by the assistance of photothermal reduction. Assisted by the high photothermal conversion efficiency of defective TiO_x (259.3 °C), the photothermal co-catalytic methane yield of Ru-TiO_x reaches 15.84 mmol/g/h with high selectivity (99.99%). After comparing the methane yields in different wavelengths, the synergistic effect between photocatalysis and thermocatalysis of Ru-TiO_x is confirmed. The theoretical calculation demonstrates that the deoxidation active sites of TiO_x and hydrogenation active sites of Ru are responsible for high activity and selectivity. Furthermore, the excellent photothermal co-catalytic activity (about 1 mmol/g/h for cloudless days) and stability under outdoor sunlight are demonstrated. This work confirms that the Ru-TiO_x system synthesized via laser bombardment has practical application value in photothermal co-catalysis of CO_2 hydrogenation.

1. Introduction

The combustion of fossil fuels in huge quantities during the economic development of human society caused the environment and energy crisis. At the same time, the global warming caused by carbon dioxide (CO_2) emissions was also worthy of attention [1,2]. It has been reported that the atmospheric CO_2 concentration has increased year by year since 1958 [3] and reached 417 ppm in 2021, which was recognized as the main reason for the greenhouse effect. Among several strategies to control CO_2 emissions, converting CO_2 into value-added chemicals/fuels of methane ($CO2 + 4H2 \rightarrow CH4 + 2H2O$, $\Delta H^{\theta}_{298, \ 1\,bar} = -165$ kJ/mol) afforded a good approach to address the above problems [4,5]. In addition, the efficient use of renewable solar energy gave a promising strategy to cope with the energy shortage issue [6,7]. Therefore, photocatalytic CO_2 hydrogenation to methane was appealing for simultaneously addressing the two issues of global warming and energy demands. However, it was noteworthy that photocatalytic CO_2 reduction faced the challenge of low fuel production rate, which limited its application for industrial scaling [8,9]. Photothermal catalysis had

great potential with high energy conversion efficiency due to the efficient utilization of the full spectrum of sunlight [10–12]. Furthermore, photothermal catalysis could also effectively mediate the activity and selectivity of CO_2 conversion by introducing specific metal catalytic sites [13,14]. For example, Ye et al. demonstrated the application of the photothermal effect for the CO_2 hydrogenation to methane using Group VIII metals [15], especially the Ru on Al_2O_3 exhibited excellent performance and high CH_4 selectivity (99.22%). In addition, Ru-loaded ultrathin layered double hydroxide catalyst (Ru@FL-LDHs) with a CH_4 selectivity of more than 99.3% was also developed for the photothermal CO_2 conversion [16]. Consequently, the presence of Ru not only boosted light absorption efficiency but also provided active sites for CO_2 hydrogenation to improve the methane selectivity.

Besides of Ru sites, the defects of oxygen vacancies in oxides could also serve as the active sites for CO_2 reduction, which facilitated the adsorption of reactive molecules during the photothermal catalysis process [17–22]. For example, Liu et al. investigated the effect of oxygen vacancy concentration in Pd/CeO_2 catalysts on the reduction of CO_2 to methanol [23]. The result demonstrated that Pd/CeO_2 with more

oxygen vacancies exhibited the highest catalytic performance, owing to the abundantly available oxygen vacancies acting as CO_2 adsorption and active sites. In addition, the oxygen vacancies significantly extended the optical adsorption range, promoting the realization of photothermal catalysis [24,25]. It was noteworthy that the construction of oxygen vacancies was generally achieved through calcination in an inert atmosphere, but the controlled regulation of oxygen vacancies and crystallization of catalysts needed more effort.

The laser bombardment has become an effective synthesis technology for nanomaterials preparation due to the advantages of low cost, scalable, fast, and permitting in-situ processing [26–29]. The metal target materials bombarded by pulsed laser generated the vapor plume composed of target atoms, ions, and clusters, which reacted with ambient gas [30] or liquid molecules [31,32] to grow nanoparticles. For example, a silver catalyst with a high density of stacking faults was prepared by laser bombardment of Ag target in a liquid, the stacking faults induced low coordination number and high tensile strain and then transformed the inactive silver into a highly active catalyst [33]. In this work, a facile and effective method to generate TiO_x nanoparticles with rich oxygen vacancies using laser bombardment of the Ti metal target under the atmosphere of Ar mixed with 0.7 vol% O_2 was designed. Using the oxygen vacancies of TiO_x and the reducing atmosphere, the uniform loading of Ru on the surface of the TiO_x nanoparticles was realized by subsequent adsorption and photothermal reduction of Ru^{3+}. The defective TiO_x nanoparticles with enhanced light absorption caused the high photothermal conversion capacity under solar light. Combined with the deoxidation active sites of TiO_x and hydrogenation active sites of Ru, a high yield (15.84 mmol/g/h) and selectivity (99.99%) of methane production from CO_2 through photothermal co-catalysis were obtained. Furthermore, an excellent photothermal catalytic activity and stability of CO_2 reduction to methane using the outdoor sunlight were demonstrated. The synthesis of defective TiO_x by laser bombardment and the application of photothermal co-catalytic CO_2 reduction had a bright application prospect in the field of CO_2 utilization.

2. Experimental

2.1. Chemicals

Ruthenium chloride hydrate ($RuCl_3·xH_2O$, 36%) was purchased from Shanghai Macklin Biochemical Co., Ltd. Titanium powders (Ti, 50 μm), Ethyl alcohol absolute (C_2H_5OH) and toluene were purchased from Sinopharm Chemical Reagents Beijing Co. Ltd. All chemicals in this work were of analytical grade without further purification. Ultrapure water (18.2 MΩ) was used in all experiments. Carbon dioxide (CO_2, purity 99.99%), oxygen (O_2, purity 99.99%), and Argon (Ar, purity 99.99%) were obtained from Jinan DeYuan Gases Co. Ltd. Hydrogen (H_2) was supplied with a CEHL-500 Hydrogen generator from Beijing China Education AuLight Technology (CEAuLight) Co., Ltd.

2.2. Synthesis of Ru nanoparticles loaded on TiO_x with oxygen vacancies (Ru-TiO_x)

Firstly, the TiO_x nanoparticles with oxygen vacancies were synthesized. A Ti metal sheet target with a diameter of 13 mm was pressed from 0.8 g commercial titanium powder by rotary tablet press under 10 MPa pressure. The TiO_x nanoparticles were generated in closed quartz container with the atmosphere of Ar/O_2 mixed gas (O_2 content of 0.7 vol%) by laser bombardment of the Ti target with a fiber laser system (LSF20D, Hgtech Laser). The pulse duration of 100 ns, laser wavelength of 1064 nm, the average power of 20 W, single pulse energy of 0.5 mJ, repetition rate of 20 kHz, scanning speed of 2000 mm s^{-1}, and scanning spacing of 0.01 mm in a back scanning mode were performed. After the laser bombardment of the Ti target, the dark blue TiO_x nanoparticles with oxygen vacancies were collected on the top of the quartz container. In comparison, the TiO_2 without oxygen defects was synthesized by laser bombardment of the Ti target in the pure O_2 atmosphere.

Second, Ru nanoparticles loaded on TiO_x (denoted as Ru-TiO_x) were synthesized. The as-obtained TiO_x powders were dispersed into an aqueous solution of 2 mM $RuCl_3$ and then stirred for 15 mins to fully absorb the Ru^{3+} ions. After centrifugation, a photothermal reduction process was performed under irradiation by a Xenon lamp (1 W/cm^2) for 1 h in the closed batch system under H_2/CO_2 mixed gas (4:1 ratio), and the black Ru-TiO_x catalyst was synthesized. Similarly, the Ru nanoparticles loaded on TiO_2 sample (Ru-TiO_2) were also prepared according to the above adsorption and photothermal reduction methods except for using TiO_2 instead of TiO_x as support.

2.3. Characterization

X-ray diffraction (XRD) (Cu Kα radiation, λ = 0.15406 nm, Rigaku Ultima IV, JPN) was used to determine the crystal structures. The morphologies and elemental distribution of the materials were characterized by field emission scanning electron microscopy (FESEM, HITACHI regulus 8100). High resolution transmission electron microscopy (HRTEM) was performed by using a JEM-2100 F instrument with an acceleration voltage of 200 kV. A High-speed video camera (X213, FuHuang Agile Device Co., Ltd) was used to observe the laser bombardment process. The chemical structure analyses of the samples were conducted by XPS (AXIS SUPRA, Kratos). Brunauer-Emmet-Teller (BET) surface area was analyzed by using a Kubo X1000 instrument using the Barrett-Joyner-Halenda (BJH) method with nitrogen adsorption at 77 K. The vacancy defects were determined by electron paramagnetic resonance (EPR) spectroscopy (Bruker A300). The UV–Vis absorption spectra and temperature distribution of samples were recorded by a UV–Vis spectrophotometer (UH4150, Hitachi High-Technologies Corporation) and Thermal Imaging Camera (Fotric 226), respectively. X-ray absorption fine structure (XAFS) measurements at the Ru K-edge for Ru-TiO_x and Ru foil samples were performed at Beijing Synchrotron Radiation Facility (beamline 1W1B station). The Ru content was determined by the Inductively Coupled Plasma Optical Emission Spectrometer (Shimadzu ICPE-9800-OES).

2.4. Photothermal co-catalytic CO_2 hydrogenation tests in the closed batch system

The experiment of photothermal co-catalytic CO_2 hydrogenation reaction was carried out in a 50 mL closed quartz reactor, and in order to maintain the temperature of the chamber, aluminum silicate fiber wool was wrapped around the reactor as an insulating layer. The typical experimental setup was shown in Fig. S1. In typical progress, 5 mg of catalysts were dispersed in 1 mL of a mixed solution of toluene and ethanol (volume ratio 3:7). Then the mixture solution was spread on the surface of a 4 cm^2 glass sheet and dried at room temperature to form a uniform coating. Before irradiation, the H_2/CO_2 mixed gas (ratio of 4:1) flow was introduced for 30 min to remove the air in the reactor and as the reactive gases. During the photothermal co-catalysis reaction, a 300 W Xenon lamp was used as the light source and heat source, which was irradiated from the top surface of the quartz reactor, giving a power density of 1 W/cm^2. To determine the temperature of the catalyst under light illumination, the infrared thermography (Infrared Thermal Imaging Camera Fotric 226) was employed. The Photoluminescence (PL) was acquired using microscopic Raman spectrometer (HORIBA LabRAM HR Evolution) with a laser of 532 nm under room temperature. During the 2 h photothermal co-catalysis reaction, the product gas was withdrawn from the reactor at 0.5 h, 1 h, 1.5 h and 2 h, and injected into the gas chromatograph for analysis. The Product rate (CO/CH$_4$yield (mol/g/h) was obtained by a linear fit of yields through time (0 ~ 2 h).

The product yield was calculated as

$$\text{Product (CO/CH}_4\text{) yield (mol/g)} = \frac{\text{Product (CO/CH}_4)_{\text{outlet}}}{m_{\text{catalyst}}}$$

Cyclic stability testing was tested using the same reactor system, after each run of 1 h, 1 mL of the reaction gas was withdrawn and the Xe light was turned off. Before the next irradiation, the reactor was evacuated and filled with the stoichiometric amounts of H_2 and CO_2 (ratio of 4:1). By analogy, the subsequent 10 recycling tests were conducted.

The pure thermal-catalytic performance was tested in the closed batch system. The reactor was evacuated and filled with the stoichiometric amounts of H_2 and CO_2 (4:1). The reactor was wrapped with a flexible electric heating jacket, the constant temperature 276 °C (Ru-TiO$_x$ catalyst).

For the photothermal co-catalytic CO_2 hydrogenation in outdoor sunlight, the 300 mL closed quartz reactor was used and the linear fresnel len (25 cm × 25 cm) was used for the sunlight concentrator.

2.5. Photoelectrochemical measurement

The photocurrent of samples was correspondingly tested by the electrochemical workstation (CHI 760 C, CH Instruments Inc.) with a three-electrode system in 0.5 M H2SO4 solution. During the photo-electrochemical testing, the Hg/Hg$_2$Cl$_2$ electrode (SCE, saturated KCl aqueous solution) was used as the reference electrode, the carbon rod was used as the counter electrode and samples modified glassy carbon electrodes were used as the working electrodes, respectively. The working electrode was prepared by the following method: 5 mg of catalyst powders were dispersed in 1 mL of water/ethanol solution (volume ratio 1:1) and then 50 μL of Nafion solution (~5% in a mixture of alcohols and water) was added. After sonication for 30 min until the mixture was well dispersed, 5 μL of the above solution was taken and dropped on the surface of glassy carbon electrode with an area of 0.07 cm^2. The photocurrent response (i-t) curves were recorded at 2 V vs. RHE in the dark and light with the light irradiation by a 300 W Xenon lamp with a power density of 1 W/cm^2.

2.6. Density functional theory (DFT) computations

The density functional theory (DFT) using the Vienna Ab-initio Simulation Package (VASP) package was utilized for first-principle calculations [34]. The generalized gradient approximation (GGA) with the Perdew−Burke−Ernzerhof (PBE) function was used to describe the correlation effects and electronic exchange [35–37]. For ensuring convergence of the total energies to within 1 meV per atom, Methfessel-Paxton electronic smearing and uniform G-centered k-points meshes with a resolution of 2 π * 0.04 Å^{-1} were adopted for the integration in the Brillouin zone for geometric optimization. The effective parameter of Coulomb interaction correction of Ti atoms, U$_{\text{eff}}$, was set as 3.5 eV [38]. The simulation was run with a cutoff energy of 500 eV throughout the computations. Structure relaxation proceeded until all forces on atoms were less than 10 meV Å^{-1} and the total stress tensor was within 0.03 GPa of the target value.
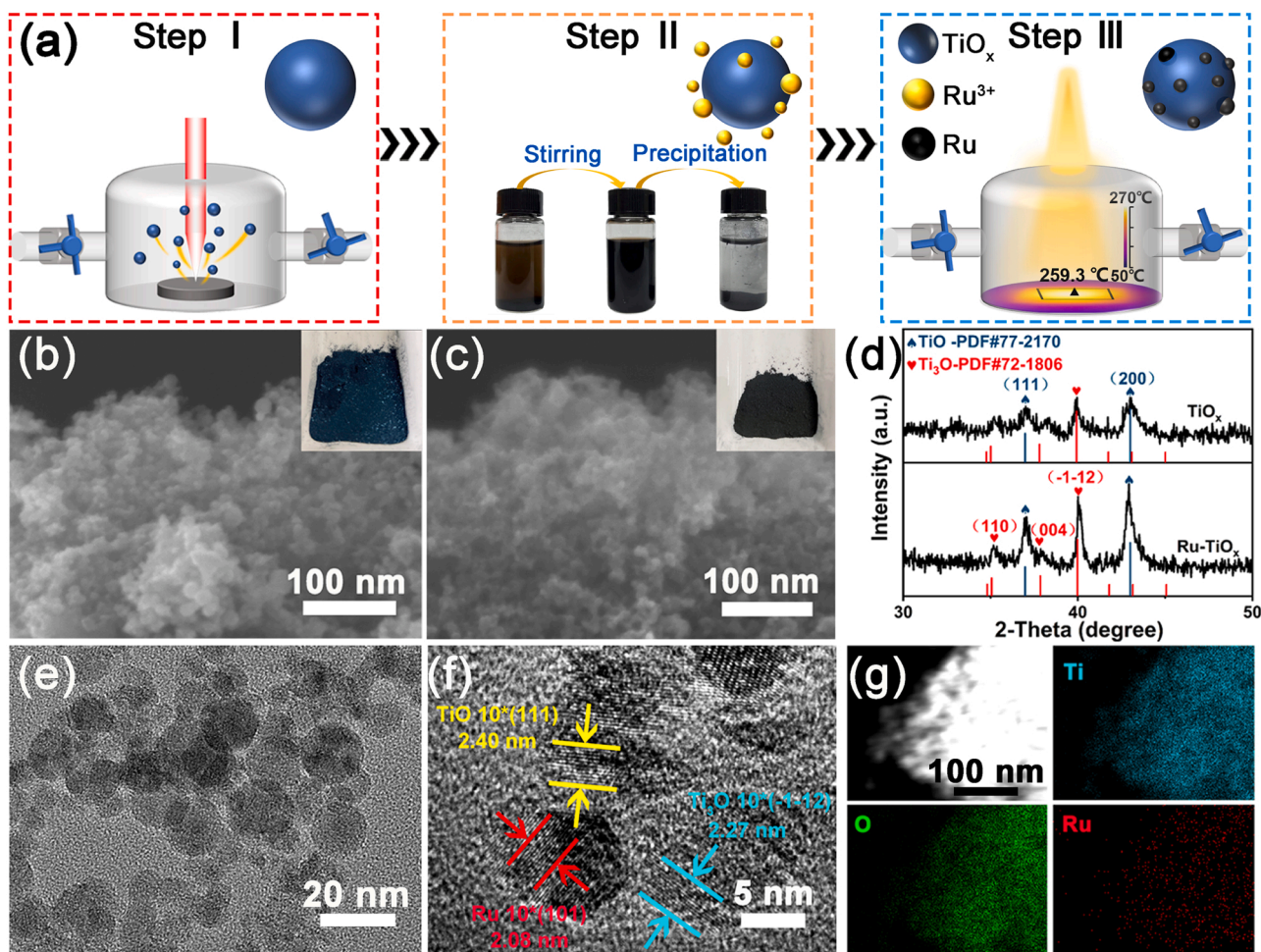

Fig. 1. (a) Illustration of the laser bombardment synthesis of TiO$_x$ nanoparticles (I), the loading of Ru on TiO$_x$ through soaking (II) and photothermal reduction process (III). SEM images and the corresponding optical photograph of (b) TiO$_x$ and (c) Ru-TiO$_x$. (d) XRD patterns of TiO$_x$ and Ru-TiO$_x$. (e, f) HRTEM images and (g) according EDS mapping of the Ru-TiO$_x$.

3. Results and discussion

3.1. Catalyst synthesis and characterizations

The synthesis process of Ru-TiO$_x$ nanoparticles was shown in Fig. 1a. Firstly, the defects-rich TiO$_x$ nanoparticles were synthesized by laser bombardment of Ti target in sealed quartz system under the mixed atmosphere (99.3 vol% Ar and 0.7 vol% O$_2$). The high-speed cameras recorded the sputtering process of nanoparticles during the laser bombardment, due to the narrow laser pulse width and high peak power (Fig. S2 and Video S1). It was noteworthy that most of the ultrafine TiO$_x$ nanoparticles (5–15 nm) moved towards the top of the container, and the large TiO$_x$ particles (100–200 nm) sank to the bottom of the container (Figs. S3 and S4). Thus, the collected ultrafine TiO$_x$ powder was characterized by SEM in Fig. 1b. The obtained TiO$_x$ powder (the inset of Fig. 1b) was dark blue, suggesting the numerous oxygen vacancies were in the TiO$_x$ nanoparticles. X-ray diffraction (XRD) results in Fig. 1d confirmed that the as-obtained TiO$_x$ nanoparticles were composed of TiO (PDF#77–2170) with the diffraction peaks at 37.1° (111) and 43.2° (200) and Ti$_3$O (PDF#72–1806) with the diffraction peak at 39.7° (−1 to 12), revealing that the defective oxidation state was formed during the laser bombardment under the anoxic atmosphere. Thus TiO$_x$ was utilized collectively to represent the mixed phase of these two titanium oxides. While TiO$_2$ composed of rutile and anatase was prepared under sufficient oxygen conditions (Fig. S6). In addition, the molar ratio of Ti/O was calculated as approximately 4:5 from the atomic percentage of each element in XPS results (Table S1). The slightly lower molar ratio of Ti/O compared with that in XRD results was probably due to the fact that XPS is a strategy of surface testing, the oxygen adsorbed on the surface resulted in more O signals.

Supplementary material related to this article can be found online at doi:10.1016/j.apcatb.2022.122176.

Secondly, the obtained TiO$_x$ nanoparticles were dispersed into an aqueous solution of 2 mM RuCl$_3$ (step II in Fig. 1a). After adding the TiO$_x$ nanoparticles, the earthy yellow Ru^{3+} aqueous solution turned colorless and black precipitate at the bottom was observed. Benefiting from the presence of oxygen vacancies and the large specific area (92.3 m^2/g, Fig. S7), the complete adsorption of Ru^{3+} ions on the surface of TiO$_x$ nanoparticles was realized (Figs. S8–S10). The photothermal reduction of Ru^{3+}-TiO$_x$ was performed by Xenon lamp under H$_2$/CO$_2$ mixed gas in the closed batch system to prepare Ru-TiO$_x$ (step III in Fig. 1a). The infrared thermal image revealed that the photothermal reduction temperature reached 259.3 °C. The optical photograph showed that the color of nanoparticles changed from dark blue to black (inset of Fig. 1c). The SEM image in Fig. 1c showed that the spherical morphology was maintained and the particle size did not increase significantly. The corresponding BET surface area of Ru-TiO$_x$ was 56.2 m^2/g (Fig. S7), less than that of TiO$_x$, due to the loading of Ru nanoparticles on the surface of TiO$_x$. XRD pattern indicated that the phases of Ru-TiO$_x$ did not change from that of TiO$_x$ (Fig. 1d) owing to the low Ru loading amount of 1.77 wt%, which was determined by inductively coupled plasma atomic emission spectrometry (ICP) (Table. S2).

In order to further demonstrate the successful reduction of Ru^{3+} to metal Ru, the transmission electron microscopy (TEM) was performed to characterize the structure of Ru-TiO$_x$. As shown in Fig. 1e, TEM image of Ru-TiO$_x$ showed that the legible nanoparticles were spherical morphology and average diameter was less than 20 nm. The lattice fringes of 0.22 nm and 0.24 nm were captured by HRTEM and attributed to the (−1 to 12) crystal plane of Ti$_3$O and the (111) crystal plane of TiO, respectively. Meanwhile, the lattice fringe of 0.20 nm attributed to (101) crystal plane of Ru was also detected in the HRTEM images (Figs. 1f and S11), demonstrating the successful Ru loading. The small particle size of prepared Ru nanoparticles could be attributed that the oxygen vacancies in TiO$_x$ acted as anchoring sites for Ru nanoparticles loading with enhanced metal-support interaction, preventing the nanoparticles from agglomeration. After statistical analysis and a frequency distribution histogram plot (Fig. S5) was generated, the diameter size of Ru nanoparticles covered the range of 1–7 nm, and there were about 61% of diameter sizes in the range of 2–3.5 nm. The formation of Ru nanoparticles with such a small particle size confirmed that Ru nanoparticles occupied the reactive oxygen vacancy sites during synthesis process.

The energy dispersive spectroscopy (EDS) elemental mapping in Fig. 1g exhibited the homogeneous distribution of the Ti, O and Ru on the nanoparticles, further implying the successful synthesis of Ru-TiO$_x$.

To gain more insight into surface chemical state and electronic structure of Ru-TiO$_x$, XPS was further examined (Fig. 2a–c). The Ti 2p spectrum (Fig. 2a) of TiO$_x$ prepared by laser bombardment could be deconvolved into three main components, which were composed of Ti^{4+}, Ti^{3+}, and Ti^{2+} as determined by the fitting of the curve at 458.3 eV, 456.2 eV and 454.2 eV, respectively [39]. After the loading of Ru nanoparticles, only XPS peaks of Ti^{4+} at 458.47 eV and Ti^{3+} at 456.81 eV could be detected. The increased peak intensity of Ti^{4+} and decreased Ti^{3+} intensity of Ru-TiO$_x$ were attributed to the reduction of Ru^{3+}, which consumed and stabilized oxygen vacancies in the photothermal reduction process of Ru-TiO$_x$. While for the TiO$_2$ prepared by laser bombardment under the oxygen-enriched environment, the high-resolution Ti 2p spectrum could only be deconvolved into two peaks of Ti 2p$_{3/2}$ at 458.4 eV and Ti 2p$_{1/2}$ at 464.1 eV for Ti^{4+}, implying that there were few oxygen vacancies. As for the O 1 s XPS spectra depicted in Fig. 2b, three peaks at 529.8 eV, 531.1 eV, and 533.2 eV, corresponding to the lattice oxygen (O$_L$), oxygen vacancy (O$_V$), and adsorbed oxygen (O$_{ad}$) were detected for TiO$_x$. After loading Ru onto TiO$_x$, the peak of oxygen vacancy (O$_V$) became less obvious, which was consumed in the photothermal reduction process [40,41]. The O 1 s spectrum of TiO$_2$ showed that the main O$_L$ peak and a negligible peak of O$_V$ were observed, due to the oxygen-enriched preparation process. The peak of Ru 3d$_{3/2}$ appeared on the same binding energy region as C 1 s peak, thus it would influence the judgment of Ru 3d$_{3/2}$ peak. As shown in Fig. 2c, the Ru 3d spectrum of Ru-TiO$_x$ showed that the binding energy of Ru 3d$_{5/2}$ peak at 279.6 eV and Ru 3d$_{3/2}$ peak at 283.4 eV attributed to Ru^0. The appearance of Ru^0 implied the successful photothermal reduction of Ru ions by reductive atmosphere with the assistance of low valent titanium in defective TiO$_x$. All of the aforementioned results proved the successful preparation of the rich-defective TiO$_x$ precursor and the successful loading of Ru on TiO$_x$. The oxygen vacancy concentration of TiO$_x$, Ru-TiO$_x$, and TiO$_2$ were evaluated by electron paramagnetic resonance (EPR) [42,43]. As shown in Fig. 2d, compared to TiO$_x$, the reduced signal of Ru-TiO$_x$ at g= 2.004 was observed, implying a partial depletion of oxygen vacancies during the loading Ru process. In contrast, the EPR result for TiO$_2$ showed no EPR signal at g= 2.004, demonstrating that the TiO$_2$ sample prepared under oxygen-enriched atmosphere contained few oxygen vacancies.

The local coordination structures and valence states of Ru-TiO$_x$ were further determined by X-ray absorption near-edge structure (XANES) spectrum and extended X-ray absorption fine structure (EXAFS) spectra. The Ru K-edge XANES spectra (Fig. 2e) showed that the Ru-TiO$_x$ was similar to Ru foil. Combined with the Fourier transform of K^3-weighted Ru EXAFS (FT-EXAFS) spectra in Fig. 2f, a characteristic peak for Ru–Ru scattering was detected in Ru-TiO$_x$, demonstrating that Ru^0 was mainly present in the material. Meanwhile, it was noteworthy that when enlarging the edge energy of Ru foil and Ru-TiO$_x$ (inset of Fig. 2e), the K-edge binding energy of Ru-TiO$_x$ was slightly larger than that of Ru foil, indicating that the average valence state of Ru-TiO$_x$ was higher. The Ru K-edge WT-EXAFS of the Ru foil and Ru-TiO$_x$ illustrated in Fig. 2g-h displayed that a significant WT signal was detected in the K (~10 Å^{-1}) and R+ α (~2.5 Å) peak, which corresponded to Ru-Ru bonds, also confirming the successful reduction and decoration of Ru nanoparticles on TiO$_x$. In addition, the weak Ru-O bond signal of Ru-TiO$_x$ could also be observed. This Ru-O bond was not attributed to RuO$_2$, while it was attributed to the Ru-O binding between Ru^0 and substrate TiO$_x$, this was in agreement with the Ru-TiO$_x$ model in Fig. S12 [44,45]. The difference
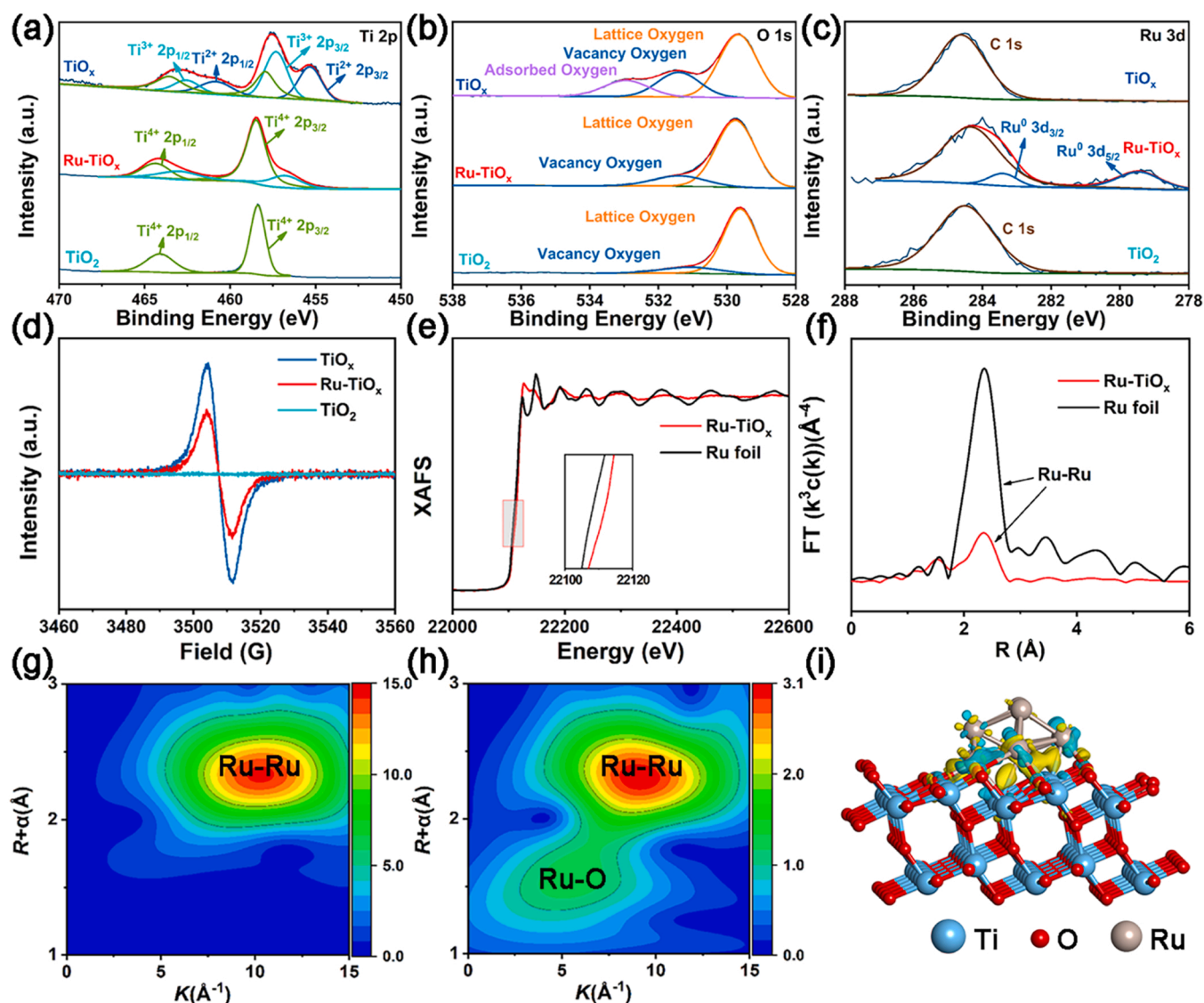
Fig. 2. XPS spectra of (a) Ti 2p, (b) O1s, and (c) Ru 3d for TiO_x, Ru-TiO_x and TiO_2. (d) Electron spin resonance spectra of TiO_x, Ru-TiO_x and TiO_2. (e) Normalized Ru K-edge XANES and (f) Fourier transform of k^3-weighted Ru EXAFS of Ru foil and Ru-TiO_x. WT-EXAFS of the Ru foil (g) and Ru-TiO_x (h). (i) Difference charge density of Ru-TiO_x (the yellow region represents the electron accumulation, while the green region represents the electron depletion).

charge density of Ru-TiO_x verified this conclusion, as shown in Fig. 2i, the electron accumulation in TiO_x indicated that the electrons transfer from Ru to TiO_x occurred due to electronegativity difference [46]. The electron transfer also indicated the strong interaction between Ru and TiO_x, which had a positive effect on the catalytic reaction.

3.2. Evaluation of photothermal co-catalytic performance

In order to study the light absorption performance, the UV–Vis–NIR absorption spectra of Ru-TiO_x, TiO_x and TiO_2 were measured as shown in Fig. 3a. For pure TiO_2, only a significant absorption in ultraviolet region was observed. Compared with TiO_2, the TiO_x and Ru-TiO_x prepared by laser bombardment exhibited much stronger light absorption capacity in the full spectrum range from UV to NIR wavelength. The oxygen vacancies in TiO_x and the plasma resonance absorption of Ru nanoparticles contributed to the high light absorption capacity from Vis to the NIR region. It was noted that the slightly stronger absorption of TiO_x than Ru-TiO_x located in the UV region and a small range of Vis region may be because that the loading of Ru nanoparticles on the surface of TiO_x would hinder the light absorption of TiO_x. The oxygen-deficient structure still existed in Ru-TiO_x, resulting in its absorption

in the IR region being unaffected. The excellent photothermal conversion ability portended the advantages of CO_2 hydrogenation [47,48]. Due to the wide wavelength range of light absorption, a strong photothermal effect was expected. The temperature profile of TiO_x, Ru-TiO_x and TiO_2 under Xenon lamp at 1 W/cm² was then tested in Fig. 3b. The measured temperature of TiO_x and Ru-TiO_x reached 259.3 °C and 276.2 °C within 1000 s, which were much higher than that of TiO_2 (84.4 °C) under the same illumination condition. In addition, the higher photothermal temperature of Ru-TiO_x compared with that of TiO_x was mainly due to the synergistic effects of TiO_x and plasma resonance absorption of Ru nanoparticles [49,50]. The according infrared thermal image captured for TiO_x, Ru-TiO_x, and TiO_2 under Xenon lamp illumination in Fig. 3c also proved the same conclusion. Especially for Ru-TiO_x, the high light-induced temperature demonstrated its potential for photothermal catalysis application, which could rapidly convert the absorbed light energy into thermal energy [51,52].

In order to further explore the role of light during the photothermal catalysis, the thermal effects of TiO_x, Ru-TiO_x and TiO_2 were tested under Xenon lamps with different light intensities (0.5, 1, 1.5 and 2 W/cm²) and different wavelengths (UV, Vis and IR irradiation). In Fig. 3d, the temperature of TiO_2 changed insignificantly under different light
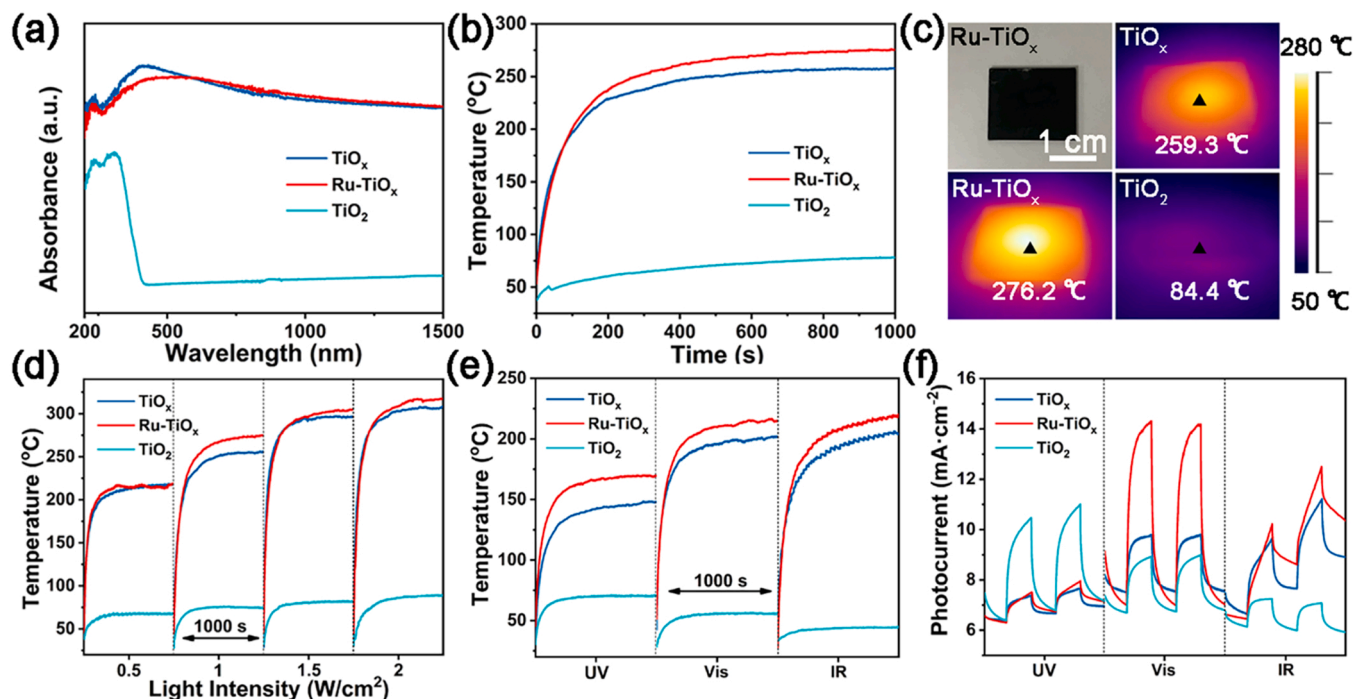
Fig. 3. (a) UV–Vis–NIR absorption spectra, (b) temperature profile, and (c) infrared thermal images of TiO_x, $Ru-TiO_x$, and TiO_2. (d) The temperature variation of the TiO_x, $Ru-TiO_x$ and TiO_2 under Xenon lamp with different light intensities. The temperature variation (e) and PEC current responses (f) of TiO_x, $Ru-TiO_x$ and TiO_2 under different light wavelengths.

intensities, with a maximum value of only 87.8 °C. For both of TiO_x and $Ru-TiO_x$, the temperature increased steadily with the increase of light intensity and could rapidly achieve the steady state, indicating the excellent photothermal conversion capacity was inseparable from the defective TiO_x. Furthermore, under the same Xenon lamp irradiation intensity of $1 W/cm^2$, the photo-induced temperature changed at different wavelengths were monitored in Fig. 3e. TiO_x and $Ru-TiO_x$ obtained higher temperatures in the visible region (202 °C and 212 °C) and infrared region (204.4 °C and 210 °C) than that in the UV region (148.4 °C and 163 °C). In a contrast, the UV region temperature (70 °C) of TiO_2 was a little bit higher than those of visible (55.8 °C) and infrared (42.2 °C) regions.

In order to further investigate the relationship between photothermal and photoelectric effects in different light regions, the verification was carried out by photocurrent tests (Fig. 3f), which was an efficient technology to evaluate the excitation of the photo-generated electron-hole pairs and characterize carrier separation. Firstly, TiO_2 produced a significantly stronger photocurrent response in the UV region than those in visible and infrared regions. Secondly, compared to TiO_2, TiOx possessed weaker photocurrent in UV region and higher photocurrent in visible and infrared regions, implying that more hot electrons were produced by TiOx. Thirdly, the Ru-TiOx possessed the enhanced photocurrent response in the visible region, confirming the synergistic effect between oxygen vacancies in TiO_x and the plasma resonance of Ru nanoparticles. The above results indicated that the presence of defective TiO_x could induce the photothermal conversion effects under vis-infrared light irradiation, while the TiO_2 mainly induced the photoelectric conversion effect under UV light irradiation. It was worth noting that the overall photocurrent response showed a gradually increasing trend under IR illumination (Fig. S13d), this may be caused by the elevated electrolyte temperature. In addition, the increasing photocurrent under each light switch was corresponding to the energy transfer between intrinsic excited photoelectrons and hot electrons. In addition, the photoluminescence (PL) spectra (Fig. S14) were performed and proved that the loading of Ru could efficiently inhibit the recombination of electron-hole pairs to improve the separation efficiency.

To reveal the advantages of $Ru-TiO_x$ in the photothermal catalytic performance, the catalytic performance tests were conducted in closed reaction system under $1 W/cm^2$ irradiation for different samples, including TiO_x, $Ru-TiO_x$, TiO_2, and $Ru-TiO_2$. To rigorously investigate the effect of oxygen vacancies on the photothermal catalytic performance, the $Ru-TiO_2$ was synthesized in the same way as $Ru-TiO_x$, just using defect-free TiO_2 as the substrate (Fig. S15). The curves of CH_4 production rate depending on the time taken were shown in Fig. S16. As shown, the CO product for TiO_x and CH_4 product for $Ru-TiO_x$ were continuously generated over time. It was noteworthy that the yields of the products increased slowly within half an hour, but showed a trend of rapid increase after half an hour of irradiation, this was possible due to the exothermic nature of the Sabatier reaction. As shown in Fig. 4a, the TiO_2 and TiO_x were more inclined to produce CO (0.067 mmol/g/h and 0.306 mmol/g/h) under the same illumination conditions. This result was consistent with the reported conclusion that the selectivity of TiO_x for CO_2 reduction was CO [53]. After loading Ru onto TiO_2 and TiO_x, the high selectivity for CH_4 was implemented. The apparent selectivity change from CO to CH_4 indicated that Ru could serve as the active site for the hydrogenation reaction of CO generated from TiO_x during the photothermal catalysis process. As for $Ru-TiO_x$, the highest CH_4 yield reached 15.84 mmol/g/h, which was approximately 176 times more than that of $Ru-TiO_2$ (0.09 mmol/g/h), indicating that the oxygen vacancies played a positive role in promoting the photothermal catalytic CO_2 hydrogenation on account of the enhanced light absorption and photothermal conversion capacity. The temperature-dependent kinetic analysis of CH_4 production rate over TiO_x and $Ru-TiO_x$ was performed. As shown in Fig. S17, the activation energy values of the overall reaction obtained from the Arrhenius plot were calculated to be 80.05 kJ $mmol^{-1}$ and 32.295 kJ $mmol^{-1}$ for TiO_x and $Ru-TiO_x$, respectively. The introduction of Ru could efficiently decrease the activation energy for Sabatier reaction. The elevated temperature through photothermal conversion had positive effect on the CO_2 conversion, which enhancing the diffusion of gas molecules and transfer of charge carriers. In addition, for TiO_x and TiO_2, the presence of oxygen vacancies in TiO_x could
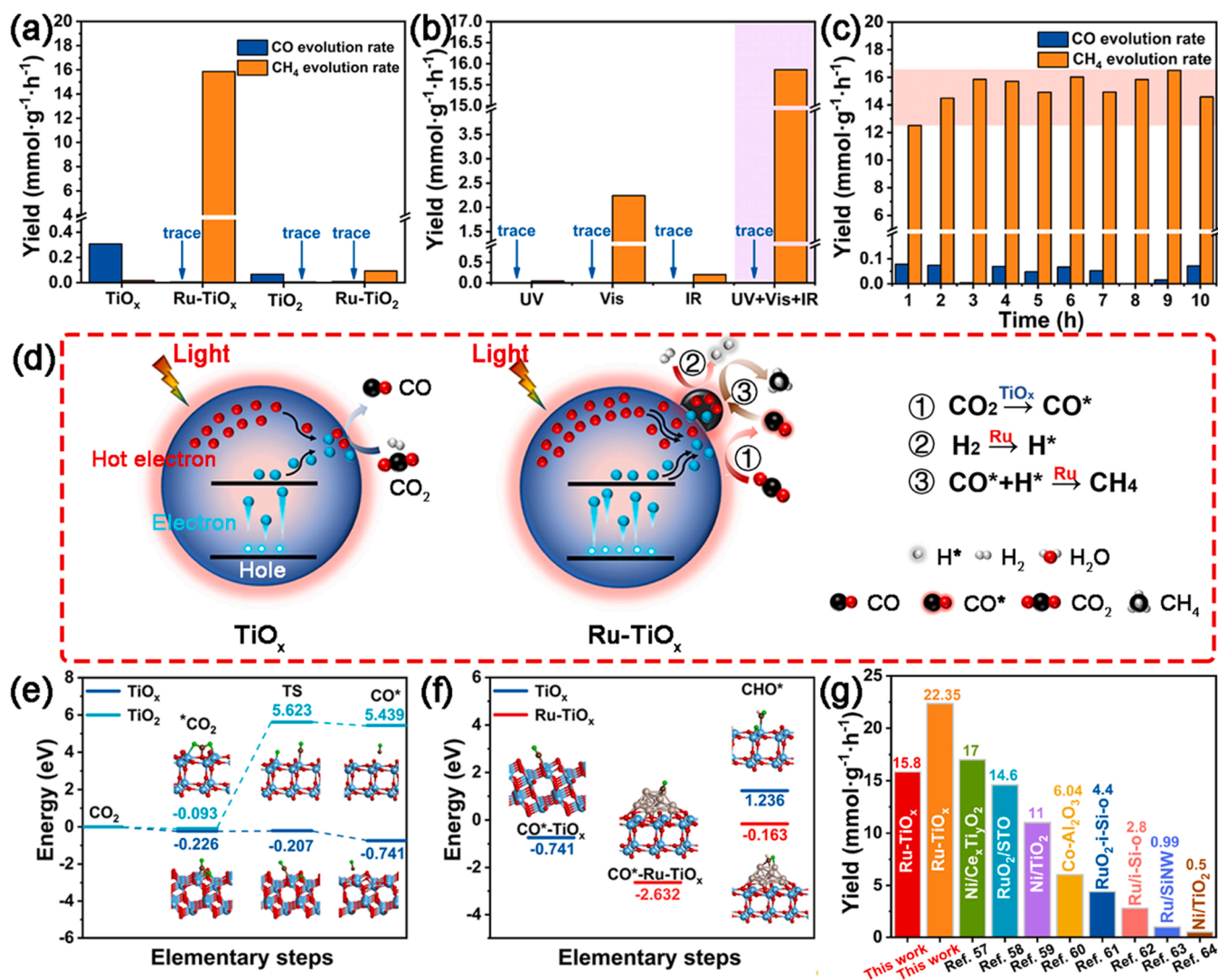
Fig. 4. (a) The yields of photothermal co-catalytic CO_2 hydrogenation for TiO_x, $Ru-TiO_x$, TiO_2, and $Ru-TiO_2$ under full-spectrum. (b) CH_4 and CO production rates of $Ru-TiO_x$ under Xenon lamp with different light wavelengths. (c) Cyclic stability testing of $Ru-TiO_x$. (d) Schematic illustration of photothermal co-catalysis CO_2 methanation for TiO_x and $Ru-TiO_x$. (e) The calculated energy change from CO_2 to CO process on TiO_2 and TiO_x. (f) Optimized structure, the CO* adsorption, and the hydrogenation reaction energy change (ΔE_{ads}) of TiO_x and $Ru-TiO_x$. (g) Comparison of CH_4 yield in this work with other recently reported photothermal catalysts.

provide more active sites for CO_2 absorption, also contributing to the great difference in photothermal property existed in TiO_x and TiO_2. Therefore, it can be concluded that the superior photothermal performance towards CO_2 conversion can be attributed to the synergetic effect of improving the diffusion of gas molecules and providing more active sites for CO_2 absorption. $^{13}CO_2$ isotope tests were conducted to confirm the source of carbon products. The isotope-labeled $^{13}CO_2$ photothermal catalytic tests screened by GC-MS was shown in Fig. S18, obvious $^{13}CH_4$ signals were detected, confirming that the carbon products were mainly generated from $^{13}CO_2$ in the photothermal catalytic CO_2 reaction. In addition, with the increased light intensity from 0.5 to 2 W/cm^2, the CH_4 evolution rate of $Ru-TiO_x$ could be further enhanced, which reached 22.35 mmol/g/h at 2 W/cm^2, as shown in Fig. S19.

To further explore the photothermal catalysis mechanism, the effect of different light wavelengths on the catalytic performance of $Ru-TiO_x$ was characterized in Fig. 4b. The negligible CH_4 yield (0.047 mmol/g/h) of $Ru-TiO_x$ under UV light irradiation was due to the relatively low photothermal temperature (163 °C). Although the temperatures of the $Ru-TiO_x$ catalyst under visible light (212 °C) and infrared light (210 °C) were similar, the methane yield of 2.25 mmol/g/h under visible irradiation was much higher than that of 0.2 mmol/g/h under infrared

irradiation, indicating the key effect of photocatalysis. In addition, the cold bath was used to exclude the thermal effect during the catalysis process (Fig. S20). The significantly decreased CH_4 yields (only μmol/g/h) were detected in all conditions, indicating the essential role of temperature during the catalysis reaction (Fig. S21). The above results indicated the synergistic effect between photocatalysis and thermocatalysis for methane production under visible light irradiation. Meanwhile, after excluding thermal effect, the increased CO selectivity and decreased CH_4 selectivity of $Ru-TiO_x$ were due to the degraded hydrogen activation at a relatively lower temperature [54]. More importantly, the catalytic performance of $Ru-TiO_x$ under full spectrum (15.84 mmol/g/h, Fig. 4a) was much higher than that under visible illumination (2.25 mmol/g/h, Fig. 4b), which further demonstrated the synergetic mechanism between photocatalysis and thermocatalysis. The conventional thermocatalysis at the same temperature of photothermal co-catalysis (276 °C) was also performed (Fig. S22). As shown, the selectivity of CO_2 hydrogenation reaction for conventional thermocatalysis remained CH_4, further confirming the effect of Ru as the hydrogenation sites. Besides, the ultra-low CH_4 yield (0.133 mmol/g_{cat}/h) of conventional thermalcatalysis was far lower than that of photothermal co-catalytic performance (15.84 mmol/g_{cat}/h), implying that this

temperature (276 °C) was a little low to exceed the thermal-dynamic barrier for CO_2 methanation. This result demonstrated that the introduction of light could break the thermodynamic equilibrium limit and realized CO_2 methanation at lower temperatures. According to the literature[55], we speculated that the light irradiation accelerated H_2 dissociation and CO_2 activation via transferring light-induced photo-generated electrons and hot electrons to d orbital of Ru atom, thereby reducing the energy barrier of the thermal catalytic reaction. In Fig. 4c, the catalytic performance of Ru-TiO_x remained stable for 10 h under 1 W/cm^2 irradiation and the according CH_4 yield remained within the range of 12.5–16.5 mmol/g/h. In addition, after the 10 h cyclic stability testing, the morphology and structure of Ru-TiO_x had no obvious change, which were confirmed by SEM, XRD, XPS, TEM, UV–Vis–NIR and EPR results in Figs. S23–S26. The XRD (Fig. S23b) result displayed the diffraction peaks of TiO and Ti_3O, which was consistent with the phase composition of sample before the cycle stability test. The remaining oxygen vacancy peak and Ti^{3+} peak in XPS (Fig. S24) results combined with the EPR result (Fig. S25) could also reveal the preservation of the defective oxidation state. The lattice fringe of 0.20 nm attributed to (101) crystal plane of Ru remain existed. And through a statistical analysis of the particle size distribution of Ru nanoparticles from HRTEM images (Figs. S27 and S28), the diameter size of most of Ru nanoparticles still covered in the range of 2–3.5 nm as the same with that before cyclic stability test, indicating the stability of Ru nanoparticles. All these results demonstrated that the catalyst in our work maintained performance and structural stability over the extended cycle stability test. In addition, the decreased catalytic stability of TiO_x shown in Fig. S29 indicated the deactivation of TiO_x due to the unstable reactive oxygen species without Ru stabilization.

Based on the above results, the catalytic mechanism of photothermal co-catalytic CO_2 reduction over the TiO_x and Ru-TiO_x were illustrated in Fig. 4d. Firstly, CO_2 was initially adsorbed by the oxygen vacancies on the TiO_x. By feat of the photothermal conversion and photoelectric effects of TiO_x, the photo-generated electrons and hot electrons were simultaneously produced and transferred to the surface of TiO_x to decompose CO_2 into CO^* and O^*. If no Ru nanoparticles were decorated, CO was produced and desorbed on account of lack of hydrogenation sites (Fig. 4d I). When loading Ru on the surface of TiO_x (Fig. 4d II), on the one hand, CO^* as the intermediate was more tendency to be adsorbed by Ru, and the transfer of CO^* from TiO_x to Ru nanoparticles was favorable for higher CO_2 reduction activity. On the other hand, under the action of irradiation, H_2 was adsorbed on Ru nanoparticles and dissociated to H atoms, which continued to participate in the subsequent hydrogenation reaction. Namely, the Ru served as the hydrogenation sites, which activated H_2 and boosted CO^* hydrogenation to produce CH_4 [56]. During this process, the photo-generated electrons and hot electrons worked together to achieve CO_2 reduction. Meanwhile, the elevated temperature through photothermal conversion had positive effect on the CO_2 conversion by enhancing the diffusion of gas molecules and transfer of charge carriers. Thus, the design-synthesized Ru-TiO_x exhibited a high CH_4 yield of 15.84 mmol/g/h and high CH_4 selectivity of 99.99% under full spectrum irradiation. For exploring the optimal matching between the oxygen vacancy content and the Ru loading, adjusting the loading amount of Ru (0.5 wt%, 2 wt% and 5 wt%) was performed and their corresponding yields of photothermal co-catalytic CO_2 hydrogenation were shown in Fig. S30, we found in the preliminary experiments that a smaller amount of Ru nanoparticle at 0.5 wt% loading resulted in a reduction in catalytic activity. While the Ru-TiO_x-2 wt% and Ru-TiO_x-5 wt% samples undergo a decrease in selectivity for methane. With the optimal Ru loading amount of 1 wt%, the highest CH_4 evolution rate and high selectivity were achieved. It may be because that a small loading amount of Ru could not provide sufficient CO_2 activation and hydrogenation active site, while an excessive loading amount of Ru may increase the size of prepared Ru nanoparticles due to the insufficient oxygen vacancy anchoring effect, as confirmed by the TEM in Fig. S31 the increased Ru nanoparticle size may

cause the decreased product selectivity by changing the reaction path.

In order to further verify the proposed photothermal co-catalytic mechanism, the first-principles density functional theory (DFT) calculations were performed. From Fig. 4e, the adsorption of CO_2 on pure TiO_2 was weak (E_{ads} = −0.093 eV), and the free energy required for its decomposition into CO^* and O^* was 5.439 eV. For the TiO_x, the adsorption ability of CO_2 on the surface was improved (E_{ads} = −0.226 eV), and the free energy required for its decomposition into CO^* and O^* was greatly reduced (−0.741 eV), indicating that the introduction of oxygen vacancies could enhance the adsorption of CO_2 and greatly reduce the decomposition energy barrier. For exploring the selectivity change from CO to CH_4, Fig. 4f displayed the CO^* adsorption and the hydrogenation reaction energy change (ΔE_{ads}) of TiO_x and Ru-TiO_x, respectively. As shown in Fig. 4f, the calculated adsorption energy of CO^* for Ru-TiO_x was − 2.632 eV, much larger than that for TiO_x, which suggested the adsorption of CO on Ru-TiO_x surface was more stable. As a consequence, after the decomposition of CO_2 to CO^* and O^* from TiO_x, the CO^* was more tendency to transfer to Ru sites. In addition, it could be seen that for TiO_x, the free energy of CO^* hydrogenation to CHO^* was 1.236 eV, while for the Ru-TiO_x, its free energy became − 0.163 eV, indicating the introduction of Ru could significantly reduce the energy barrier for CO hydrogenation. These results demonstrated that Ru as the hydrogenation active sites contributed to the selectivity change for CH_4.

For evaluating the photothermal co-catalytic performance of Ru-TiO_x, the CH_4 yields of recently reported photothermal catalysts were summarized in Fig. 4g and Table S3. The CH_4 yields of 15.84 mmol/g/h with 99.99% of CH_4 selectivity at 1 W/cm^2 and 22.35 mmol/g/h at 2 W/cm^2 for Ru-TiO_x without external heating and pressure were better than or comparable to the reported catalysts, such as Ni/$Ce_xTi_yO_2$ (17 mmol/g/h) [57], RuO_2/STO (14.6 mmol/g/h) [58], Ni/TiO_2 (11 mmol/g/h) [59], Co/Al_2O_3 (6.04 mmol/g/h) [60], RuO_2/3D silicon (4.4 mmol/g/h) [61], Ru inverted silicon opal photonic crystal (Ru/i-Si-o) (2.8 mmol/g/h) [62], Ru/Si NW (0.99 mmol/g/h) [63] and Ni/TiO_2 (0.504 mmol/g/h) [64].

3.3. Photothermal co-catalysis system under the outdoor sunlight

To demonstrate the practical applicability of Ru-TiO_x, the photothermal co-catalytic CO_2 hydrogenation was conducted by using the outdoor sunlight as light source and heat source. The photothermal co-catalysis device composed of closed quartz reactor, aluminum silicate fiber wool, and the linear fresnel len (25 cm × 25 cm) was constructed (Fig. 5a), where the linear fresnel len was used for the sunlight concentrator. Infrared thermal images showed that the Ru-TiO_x as catalyst reached 203.2 °C when the sunlight was focused on the catalyst (Fig. S33). The aluminum silicate fiber wool wrapped around the reactor was used for maintaining the temperature of the chamber. By using H_2/CO_2 gas mixture with a ratio of 4:1 as the reactive gases. The activity and stability of photothermal co-catalysis CO_2 hydrogenation were conducted at 11:00–12:00 every day for seven consecutive days. The according weather and temperature at that time were recorded in inset of Fig. 5b. When the weather was cloudless from Sunday to Thursday, the CH_4 production rates basically stayed at about 0.95–1.12 mmol/g/h. When the weather was cloudy on Friday, the photothermal co-catalytic performance decreased, but it still achieved a methane yield of about 0.54 mmol/g/h. The high photothermal co-catalytic performance of CO_2 hydrogenation confirmed that the Ru-TiO_x synthesized from laser bombardment had the potential for practical application.

4. Conclusions

A facile and effective laser bombardment method to generate TiO_x nanoparticles with oxygen vacancies was developed. The TiO_x nanoparticles as efficient carrier could uniformly load ultrafine Ru nanoparticles with the assistance of photothermal reduction. The defective
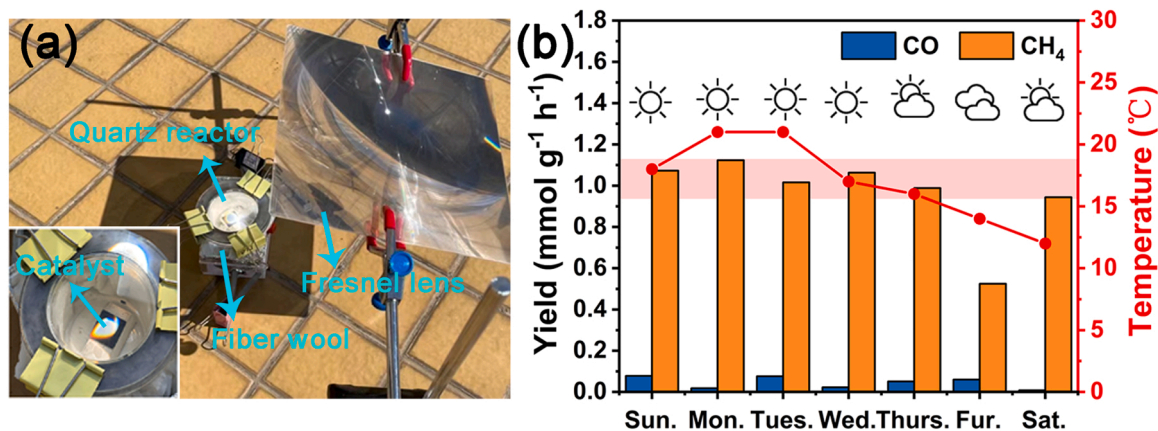
Fig. 5. (a) Illustration photograph of constructed photothermal co-catalysis device using the outdoor sunlight. (b) The recorded day's yields of CH_4 and CO for Ru-TiO_x in consecutive week (11:00–12:00 a.m.).

TiO_x nanoparticles had the functions of both photothermal conversion and photoelectric conversion, which realized the reduction of CO_2 into CO* . And then Ru nanoparticles acted as the hydrogenation site to adsorb intermediate CO* and activate hydrogen. The synergistic effect between the deoxidation active sites of TiO_x and hydrogenation active sites of Ru realized a high CH_4 yield (15.84 mmol/g/h) and selectivity (99.99%) for design-synthesized Ru-TiO_x under full spectrum irradiation. Furthermore, we performed the photothermal co-catalysis of CO_2 reduction to methane under the outdoor sunlight, an excellent catalytic activity (about 1 mmol/g/h for cloudless days) and stability (at 11:00–12:00 for seven consecutive days) in real situations were demonstrated, verifying the practical applicability of our system.

CRediT authorship contribution statement

Tianjiao Dong: Data curation, Formal analysis, Investigation, Visualization, Formal analysis, Investigation. **Xiaoyu Liu:** Data curation, Methodology, Validation, Writing – review & editing. **Zhenfei Tang**: Supervision, Validation. **Haifeng Yuan:** Supervision, Validation. **Di Jiang:** Supervision, Validation. **Yijie Wang:** Supervision, Validation. **Zhen Liu:** Supervision, Validation. **Xiaoli Zhang:** Supervision, Validation. **Shifeng Huang**: Supervision, Validation. **Hong Liu:** Project administration, Resources, Supervision, Validation. **Lili Zhao:** Data curation, Funding acquisition, Methodology, Validation, Writing – review & editing. **Weijia Zhou:** Conceptualization, Funding acquisition, Project administration, Resources, Supervision, Writing – review & editing.

Declaration of Competing Interest

The authors declare that they have no known competing financial interests or personal relationships that could have appeared to influence the work reported in this paper.

Data Availability

The authors do not have permission to share data.

Acknowledgments

Appendix A. Supporting information

Supplementary data associated with this article can be found in the online version at doi:10.1016/j.apcatb.2022.122176.

References

[1] Y. Wang, Y. Chen, Y. Zhao, J. Yu, Z. Liu, Y. Shi, H. Liu, X. Li, W. Zhou, Laser-fabricated channeled Cu_6Sn_5/Sn as electrocatalyst and gas diffusion electrode for efficient CO_2 electroreduction to formate, Appl. Catal. B Environ. 307 (2021), 120991, https://doi.org/10.1016/j.apcatb.2021.120991.

[2] L. Chang, D.J. Stacchiola, Y.H. Hu, An ideal electrode material, 3D surface-microporous graphene for supercapacitors with ultrahigh areal capacitance, ACS Appl. Mater. Interfaces 9 (2017) 24655–24661, https://doi.org/10.1021/acsami.7b07381.

[3] Z.J. Wang, H. Song, H. Liu, J. Ye, Coupling of solar energy and thermal tnergy for carbon dioxide reduction: status and prospects, Angew. Chem. Int. Ed. 59 (2020) 8016–8035, https://doi.org/10.1002/anie.201907443.

[4] L.L. Lin, K. Wang, K. Yang, X. Chen, X.Z. Fu, W.X. Dai, The visible-light-assisted thermocatalytic methanation of CO_2 over Ru/$TiO_{(2-X)}N_X$, Appl. Catal. B Environ. 204 (2017) 440–455, https://doi.org/10.1016/j.apcatb.2016.11.054.

[5] B. Jin, X. Ye, H. Zhong, F. Jin, Y.H. Hu, Enhanced photocatalytic CO_2 hydrogenation with wide-spectrum utilization over black TiO_2 supported catalyst, Chin. Chem. Lett. 33 (2022) 812–816, https://doi.org/10.1016/j.cclet.2021.07.046.

[6] Y. Ma, Q. Tang, W.-Y. Sun, Z.-Y. Yao, W. Zhu, T. Li, J. Wang, Assembling ultrafine TiO_2 nanoparticles on UiO-66 octahedrons to promote selective photocatalytic conversion of CO_2 to CH_4 at a low concentration, Appl. Catal. B Environ. 270 (2020), https://doi.org/10.1016/j.apcatb.2020.118856.

[7] Y. Ma, X. Yi, S. Wang, T. Li, B. Tan, C. Chen, T. Majima, E.R. Waclawik, H. Zhu, J. Wang, Selective photocatalytic CO_2 reduction in aerobic environment by microporous Pd-porphyrin-based polymers coated hollow TiO_2, Nat. Commun. 13 (2022) 1400, https://doi.org/10.1038/s41467-022-29102-0.

[8] M. Ghoussoub, M.K. Xia, P.N. Duchesne, D. Segal, G. Ozin, Principles of photothermal gas-phase heterogeneous CO_2 catalysis, Energy Environ. Sci. 12 (2019) 1122–1142, https://doi.org/10.1039/C8EE02790K.

[9] G. Yang, P. Qiu, J. Xiong, X. Zhu, G. Cheng, Facilely anchoring Cu_2O nanoparticles on mesoporous TiO_2 nanorods for enhanced photocatalytic CO_2 reduction through efficient charge transfer, Chin. Chem. Lett. 33 (2021) 3709–3712, https://doi.org/10.1016/j.cclet.2021.10.047.

[10] Y. Zhu, S. Chen, S. Fang, Z. Li, C. Wang, Y.H. Hu, Distinct pathways in visible-light driven thermo-photo catalytic methane conversion, J. Phys. Chem. Lett. 12 (2021) 7459–7465, https://doi.org/10.1021/acs.jpclett.1c02053.

[11] M. Li, Z. Sun, Y.H. Hu, Thermo-photo coupled catalytic CO_2 reforming of methane: a review, Chem. Eng. J. 428 (2022), 131222, https://doi.org/10.1016/j.cej.2021.131222.

[12] M. Xu, X. Hu, S. Wang, J. Yu, D. Zhu, J. Wang, Photothermal effect promoting CO_2 conversion over composite photocatalyst with high graphene content, J. Catal. 377 (2019) 652–661, https://doi.org/10.1016/j.jcat.2019.08.010.

[13] X. Wang, X. Zou, Z. Rui, Y. Wang, H. Ji, Highly dispersed and active Pd nanoparticles over titania support through engineering oxygen vacancies and their anchoring effect, AIChE J. 66 (2020), https://doi.org/10.1002/aic.16288.

[14] J. Chen, X. Wang, L. Zhang, Z. Rui, Strong metal-support interaction assisted redispersion strategy for obtaining ultrafine and stable $IrO2$/Ir active sites with exceptional methane oxidation activity, Appl. Catal. B Environ. 297 (2021), https://doi.org/10.1016/j.apcatb.2021.120410.

[15] X. Meng, T. Wang, L. Liu, S. Ouyang, P. Li, H. Hu, T. Kako, H. Iwai, A. Tanaka, J. Ye, Photothermal conversion of CO_2 into CH_4 with H_2 over Group VIII

nanocatalysts: an alternative approach for solar fuel production, Angew. Chem. Int. Ed. 53 (2014) 11478–11482, https://doi.org/10.1002/anie.201404953.

[16] J. Ren, S. Ouyang, H. Xu, X. Meng, T. Wang, D. Wang, J. Ye, Targeting activation of CO₂ and H₂ over Ru-loaded ultrathin layered double hydroxides to achieve efficient photothermal CO₂ methanation in flow-type system, Adv. Energy Mater. 7 (2017) 1601657, https://doi.org/10.1002/aenm.201601657.

[17] J. Kang, Y. Zhang, Z. Chai, X. Qiu, X. Cao, P. Zhang, G. Teobaldi, L.M. Liu, L. Guo, Amorphous domains in black titanium dioxide, Nat. Commun. 33 (2021), e2100407, https://doi.org/10.1002/adma.202100407.

[18] Q.Y. Bi, K.Y. Hu, J.C. Chen, Y.R. Zhang, M.S. Riaz, J. Xu, Y.F. Han, F.Q. Huang, Black phosphorus coupled black titania nanocomposites with enhanced sunlight absorption properties for efficient photocatalytic CO₂ reduction, Appl. Catal. B Environ. 295 (2021), 120211, https://doi.org/10.1016/j.apcatb.2021.120211.

[19] H.H. Wei, X.G. Ma, L. Gu, J.Q. Li, W.J. Si, G. Ou, W. Yu, C.S. Zhao, J.Y. Li, M. J. Song, Z.J. Peng, H. Wu, Aerodynamic levitated laser annealing method to defective titanium dioxide with enhanced photocatalytic performance, Nano Res. 9 (2016) 3839–3847, https://doi.org/10.1007/s12274-016-1253-0.

[20] J. Wang, G. Zhang, J. Zhu, X. Zhang, F. Ding, A. Zhang, X. Guo, C. Song, CO₂ hydrogenation to methanol over In₂O₃-based catalysts: from mechanism to catalyst development, ACS Catal. 11 (2021) 1406–1423, https://doi.org/10.1021/acscatal.0c03665.

[21] X. Bian, S. Zhang, Y. Zhao, R. Shi, T. Zhang, Layered double hydroxide-based photocatalytic materials toward renewable solar fuels production, InfoMat 3 (2021) 719–738, https://doi.org/10.1002/inf2.12192.

[22] Y. Wu, Y. Li, J. Gao, Q. Zhang, Recent advances in vacancy engineering of metal-organic frameworks and their derivatives for electrocatalysis, SusMat 1 (2021) 66–87, https://doi.org/10.1002/sus2.3.

[23] F. Jiang, S. Wang, B. Liu, J. Liu, L. Wang, Y. Xiao, Y. Xu, X. Liu, Insights into the influence of CeO₂ crystal facet on CO₂ hydrogenation to methanol over Pd/CeO₂ catalysts, ACS Catal. 10 (2020) 11493–11509, https://doi.org/10.1021/acscatal.0c03324.

[24] C. Wang, S. Fang, S. Xie, Y. Zheng, Y.H. Hu, Thermo-photo catalytic CO₂ hydrogenation over Ru/TiO₂, J. Mater. Chem. A 8 (2020) 7390–7394, https://doi.org/10.1039/c9ta13275a.

[25] J. Li, J. Feng, X. Guo, H. Fang, J. Chen, C. Ma, R. Li, Y. Wang, Z. Rui, Defect-band bridge thermally activates type III heterojunction for CO₂ reduction and typical VOCs oxidation, Appl. Catal. B Environ. 309 (2022), https://doi.org/10.1016/j.apcatb.2022.121248.

[26] J. Bian, L. Zhou, X. Wan, C. Zhu, B. Yang, Y. Huang, Laser transfer, printing, and assembly techniques for flexible electronics, Adv. Electron. Mater. 5 (2019) 1800900, https://doi.org/10.1002/aelm.201800900.

[27] H. Palneedi, J.H. Park, D. Maurya, M. Peddigari, G.T. Hwang, V. Annapureddy, J. W. Kim, J.J. Choi, B.D. Hahn, S. Priya, K.J. Lee, J. Ryu, Laser irradiation of metal oxide films and nanostructures: applications and advances, Adv. Mater. 30 (2018), e1705148, https://doi.org/10.1002/adma.201705148.

[28] Y. Park, D. Yoon, K. Fukutani, R. Stania, J. Son, Steep-slope threshold switch enabled by pulsed-laser-induced phase transformation, ACS Appl. Mater. Interfaces 11 (2019) 24221–24229, https://doi.org/10.1021/acsami.9b04015.

[29] L. Li, J. Zhang, Y. Wang, F.U. Zaman, Y. Zhang, L. Hou, C. Yuan, Laser irradiation construction of nanomaterials toward electrochemical energy storage and conversion: ongoing progresses and challenges, InfoMat 3 (2021) 1393–1421, https://doi.org/10.1002/inf2.12218.

[30] G. Ou, P. Fan, H. Zhang, K. Huang, C. Yang, W. Yu, H. Wei, M. Zhong, H. Wu, Y. Li, Large-scale hierarchical oxide nanostructures for high-performance electrocatalytic water splitting, Nano Energy 35 (2017) 207–214, https://doi.org/10.1016/j.nanoen.2017.03.049.

[31] S.O. Gurbatov, E. Modin, V. Puzikov, P. Tonkaev, D. Storozhenko, A. Sergeev, N. Mintcheva, S. Yamaguchi, N.N. Tarasenka, A. Chuvilin, S. Makarov, S. A. Kulinich, A.A. Kuchmizhak, Black Au-decorated TiO₂ produced via laser ablation in liquid, ACS Appl. Mater. Interfaces 13 (2021) 6522–6531, https://doi.org/10.1021/acsami.0c20463.

[32] R.C. Forsythe, C.P. Cox, M.K. Wilsey, A.M. Muller, Pulsed laser in liquids made nanomaterials for catalysis, Chem. Rev. 121 (2021) 7568–7637, https://doi.org/10.1021/acs.chemrev.0c01069.

[33] Z. Li, J.-Y. Fu, Y. Feng, C.-K. Dong, H. Liu, X.-W. Du, A silver catalyst activated by stacking faults for the hydrogen evolution reaction, Nat. Catal. 2 (2019) 1107–1114, https://doi.org/10.1038/s41929-019-0365-9.

[34] G. Kresse, J. Furthmüller, Efficiency of ab-initio total energy calculations for metals and semiconductors using a plane-wave basis set, Comput. Mater. Sci. 6 (1996) 15–50, https://doi.org/10.1016/0927-0256(96)00008-0.

[35] J.P. Perdew, K. Burke, M. Ernzerhof, Generalized gradient approximation made simple, Phys. Rev. Lett. 77 (1996) 3865–3868, https://doi.org/10.1103/PhysRevLett.77.3865.

[36] P.E. Blochl, Projector augmented-wave method, Phys. Rev. B Condens. Matter 50 (1994) 17953–17979, https://doi.org/10.1103/PhysRevB.50.17953.

[37] G. Kresse, D. Joubert, From ultrasoft pseudopotentials to the projector augmented-wave method, Phys. Rev. B 59 (1999) 1758–1775, https://doi.org/10.1103/PhysRevB.59.1758.

[38] J.-Y. Liu, X.-Q. Gong, A.N. Alexandrova, Mechanism of CO₂ photocatalytic reduction to methane and methanol on defected anatase TiO₂ (101): a density functional theory study, J. Phys. Chem. C 123 (2019) 3505–3511, https://doi.org/10.1021/acs.jpcc.8b09539.

[39] Q. Han, C. Wu, H. Jiao, R. Xu, Y. Wang, J. Xie, Q. Guo, J. Tang, Rational design of high-concentration Ti³⁺ in porous carbon-doped TiO₂ nanosheets for efficient photocatalytic ammonia synthesis, Adv. Mater. 33 (2021) 2008180, https://doi.org/10.1002/adma.202008180.

[40] Y. Zhao, Y. Zhao, R. Shi, B. Wang, G.I.N. Waterhouse, L.Z. Wu, C.H. Tung, T. Zhang, Tuning oxygen vacancies in ultrathin TiO₂ nanosheets to boost photocatalytic nitrogen fixation up to 700 nm, Adv. Mater. 31 (2019) 1806482, https://doi.org/10.1002/adma.201806482.

[41] C. Li, T. Wang, Z.J. Zhao, W. Yang, J.F. Li, A. Li, Z. Yang, G.A. Ozin, J. Gong, Promoted fixation of molecular nitrogen with surface oxygen vacancies on plasmon-enhanced TiO₂ photoelectrodes, Angew. Chem. Int. Ed. 57 (2018) 5278–5282, https://doi.org/10.1002/anie.201713229.

[42] G. Ou, Y. Xu, B. Wen, R. Lin, B. Ge, Y. Tang, Y. Liang, C. Yang, K. Huang, D. Zu, R. Yu, W. Chen, J. Li, H. Wu, L.M. Liu, Y. Li, Tuning defects in oxides at room temperature by lithium reduction, Nat. Commun. 9 (2018) 1302, https://doi.org/10.1038/s41467-018-03765-0.

[43] M. Wajid Shah, Y. Zhu, X. Fan, J. Zhao, Y. Li, S. Asim, C. Wang, Facile synthesis of defective TiO₂₋ₓ nanocrystals with high surface area and tailoring bandgap for visible-light photocatalysis, Sci. Rep. 5 (2015) 15804, https://doi.org/10.1038/srep15804.

[44] H. Zhang, S. Zuo, M. Qiu, S. Wang, Y. Zhang, J. Zhang, X.W.D. Lou, Direct probing of atomically dispersed Ru species over multi-edged TiO₂ for highly efficient photocatalytic hydrogen evolution, Sci. Adv. 6 (2020), https://doi.org/10.1126/sciadv.abb9823.

[45] S. Hao, M. Liu, J. Pan, X. Liu, X. Tan, N. Xu, Y. He, L. Lei, X. Zhang, Dopants fixation of ruthenium for boosting acidic oxygen evolution stability and activity, Nat. Commun. 11 (2020) 5368, https://doi.org/10.1038/s41467-020-19212-y.

[46] X. Liu, C. Xing, F. Yang, Z. Liu, Y. Wang, T. Dong, L. Zhao, H. Liu, W. Zhou, Strong interaction over ru/defects-rich aluminium oxide boosts photothermal CO₂ methanation via microchannel flow-type system, Adv. Energy Mater. (2022) 2201009, https://doi.org/10.1002/aenm.202201009.

[47] E.T. Kho, T.H. Tan, E. Lovell, R.J. Wong, J. Scott, R. Amal, A review on photo-thermal catalytic conversion of carbon dioxide, Green Energy Environ. 2 (2017) 204–217, https://doi.org/10.1016/j.gee.2017.06.003.

[48] X. Wang, J.A. Rodriguez, J.C. Hanson, D. Gamarra, A. Martínez-Arias, M. Fernández-García, In situ studies of the active sites for the water gas shift reaction over Cu–CeO₂ catalysts: complex interaction between metallic copper and oxygen vacancies of ceria, J. Phys. Chem. B 110 (2005) 428–434, https://doi.org/10.1021/jp055467g.

[49] J. Li, J. Chen, H. Fang, X. Guo, Z. Rui, Plasmonic metal bridge leading type III heterojunctions to robust type B photothermocatalysts, Ind. Eng. Chem. Res. 60 (2021) 8420–8429, https://doi.org/10.1021/acs.iecr.1c01198.

[50] J. Li, X. Yang, C. Ma, Y. Lei, Z. Cheng, Z. Rui, Selectively recombining the photoinduced charges in bandgap-broken Ag3PO4/GdCrO3 with a plasmonic Ag bridge for efficient photothermocatalytic VOCs degradation and CO₂ reduction, Appl. Catal. B Environ. 291 (2021), https://doi.org/10.1016/j.apcatb.2021.120053.

[51] Y. Qi, L. Song, S. Ouyang, X. Liang, S. Ning, Q. Zhang, J. Ye, Photoinduced defect engineering: enhanced photothermal catalytic performance of 2D black In₂O₃₋ₓ nanosheets with bifunctional oxygen vacancies, Adv. Mater. 32 (2020) 1903915, https://doi.org/10.1002/adma.201903915.

[52] X. Hu, Z. Xie, Q. Tang, H. Wang, L. Zhang, J. Wang, Enhanced CH4 yields by interfacial heating-induced hot water steam during photocatalytic CO₂ reduction, Appl. Catal. B Environ. 298 (2021), https://doi.org/10.1016/j.apcatb.2021.120635.

[53] Y. Li, C. Wang, M. Song, D. Li, X. Zhang, Y. Liu, TiO₂₋ₓ/CoOₓ photocatalyst sparkles in photothermocatalytic reduction of CO₂ with H₂O steam, Appl. Catal. B Environ. 243 (2019) 760–770, https://doi.org/10.1016/j.apcatb.2018.11.022.

[54] H. Liu, L. Shi, Q. Zhang, P. Qi, Y. Zhao, Q. Meng, X. Feng, H. Wang, J. Ye, Photothermal catalysts for hydrogenation reactions, ChemComm 57 (2021) 1279–1294, https://doi.org/10.1039/D0CC07144G.

[55] Y. Li, Z. Liu, Z. Rao, Z. Yu, F. Wang, Y. Tang, H. Zhao, J. Zhang, Z. Wang, J. Li, Z. Huang, Y. Zhou, Y. Li, B. Dai, Experimental and theoretical insights into an enhanced CO₂ methanation mechanism over a Ru-based catalyst, Appl. Catal. B Environ. 319 (2022), https://doi.org/10.1016/j.apcatb.2022.121903.

[56] Y. Chen, Y.M. Zhang, G.Z. Fan, L.Z. Song, G. Jia, H.T. Huang, S.X. Ouyang, J.H. Ye, Z.S. Li, Z.G. Zou, Cooperative catalysis coupling photo-/photothermal effect to drive Sabatier reaction with unprecedented conversion and selectivity, Joule 5 (2021) 3235–3251, https://doi.org/10.1016/j.joule.2021.11.009.

[57] E.T. Kho, S. Jantarang, Z. Zheng, J. Scott, R. Amal, Harnessing the beneficial attributes of ceria and titania in a mixed-oxide support for nickel-catalyzed photothermal CO₂ methanation, Engineering 3 (2017) 393–401, https://doi.org/10.1016/j.ENG.2017.03.016.

[58] D. Mateo, J. Albero, H. Garcia, Titanium-perovskite-supported RuO₂ nanoparticles for photocatalytic CO₂ methanation, Joule 3 (2019) 1949–1962, https://doi.org/10.1016/j.joule.2019.06.001.

[59] D. Mateo, N. Morlanes, P. Maity, G. Shterk, O.F. Mohammed, J. Gascon, Efficient visible-light driven photothermal conversion of CO₂ to methane by nickel nanoparticles supported on barium titanate, Adv. Funct. Mater. 31 (2020) 2008244, https://doi.org/10.1002/adfm.202008244.

[60] X. Chen, Q. Li, M. Zhang, J. Li, S. Cai, J. Chen, H. Jia, MOF-templated preparation of highly dispersed Co/Al₂O₃ composite as the photothermal catalyst with high solar-to-fuel efficiency for CO₂ methanation, ACS Appl. Mater. Interfaces 12 (2020) 39304–39317, https://doi.org/10.1021/acsami.0c11576.

[61] A.A. Jelle, K.K. Ghuman, P.G. O'Brien, M. Hmadeh, A. Sandhel, D.D. Perovic, C. V. Singh, C.A. Mims, G.A. Ozin, Highly efficient ambient temperature CO₂ photomethanation catalyzed by nanostructured RuO₂ on silicon photonic crystal support, Adv. Energy Mater. 8 (2018) 1702277, https://doi.org/10.1002/aenm.201702277.

[62] P.G. O'Brien, K.K. Ghuman, A.A. Jelle, A. Sandhel, T.E. Wood, J.Y.Y. Loh, J. Jia, D. Perovic, C.V. Singh, N.P. Kherani, C.A. Mims, G.A. Ozin, Enhanced photothermal reduction of gaseous CO_2 over silicon photonic crystal supported ruthenium at ambient temperature, Energy Environ. Sci. 11 (2018) 3443–3451, https://doi.org/10.1039/C8EE02347F.

[63] P.G. O'Brien, A. Sandhel, T.E. Wood, A.A. Jelle, L.B. Hoch, D.D. Perovic, C. A. Mims, G.A. Ozin, Photomethanation of gaseous CO_2 over Ru/silicon nanowire catalysts with visible and near-infrared photons, Adv. Sci. 1 (2014) 1400001, https://doi.org/10.1002/advs.201400001.

[64] Q. Li, Y.X. Gao, M. Zhang, H. Gao, J. Chen, H.P. Jia, Efficient infrared-light-driven photothermal CO_2 reduction over MOF-derived defective Ni/TiO_2, Appl. Catal. B Environ. 303 (2022), 120905, https://doi.org/10.1016/j.apcatb.2021.120905.